PCCP

Accepted Manuscript

ROYAL SOCIETY OF CHEMISTRY

www.rsc.org/pccp

Fingerprints of Short-Range and Long-Range Structure in $BaZr_{1-x}Hf_xO_3$ Solid Solutions: An Experimental and Theoretical Study†

Rafael Uarth Fassbender,[a] Tatiane Strelow Lilge,[a] Sergio Cava,[b] Juan Andrés,[c] Luis Fernando da Silva,[d] Valmor Roberto Mastelaro,[d] Elson Longo, [e] Mario Lucio Moreira,*[a]

Received Xth XXXXXXXXXX 20XX, Accepted Xth XXXXXXXXX 20XX

First published on the web Xth XXXXXXXXXX 200X

DOI: 10.1039/b000000x

Microwave-assisted hydrothermal method was applied to synthesize $BaZr_{1-x}Hf_xO_3$, (BZHO) solid solutions at low temperature, 140°C, and relative short times, 160 min. The detailed features of the crystal structure, at both short and long ranges, as well as the crystal chemistry doping process, are extensively analysed. X-ray diffraction measurements and Raman spectroscopy have been used to confirm that pure and Hf-doped BZO materials present a cubic structure. Extended X-ray absorption fine structure (EXAFS) indicate that Hf^{4+} ions has replaced the Zr^{4+} ions on the 6-fold coordination and a subsequent change on the Ba^{2+} 12-fold coordination can be sensed. X-ray absorption near-edge spectroscopy (XANES) measurements reveal a local symmetry breaking process, associated to overlap of the 4d – 2p and 5d – 2p orbitals of Zr-O and Hf-O bonds, respectively. Field emission gun (FE-SEM) and high resolution transmission electron microscope (HRTEM) show the mesocrystalline nature of self-assembled BZHO nanoparticles under dodecahedron shape. In addition were performed first principle calculations to complement experimental data. The analysis of the band structures and density of states of undoped BZO and doped BZHO host lattice allow a deep insight on the main electronic features. The theoretical results help us to find a correlation between simulated and experimental Raman modes and allow a more substantial interpretation of crystal structure.

1 Introduction

The modern scientific research is constantly looking to innovations and it could not be different for highly promising systems as perovskite based materials[1–3].

As a typical perovskite material, barium zirconate ($BaZrO_3$, BZO) is of both fundamental interest and practical importance in many applications. This material is chemically and thermally stable[4,5], as well as their optical properties were observed under different circumstances, since quasi-amorphous compounds[6] through quasi-crystalline systems[6,7] and finally to periodic crystals[8,9]. BZO presents cubic perovskite symmetry with ZrO_6 octahedral and BaO_{12} cubooctahedral clusters. All individual or conjugated clusters contributing to both electronic and optical properties such as a high dielectric constant and a reasonable wide band-gap around ∼ 5.4 eV[10], which are important properties for energy related applications. In particular, these properties have made possible the BZO application as superconductor pinning centers[11,12] to improve the typical superconductive features. Recently, Borja-Urby et. al. reported the photocatalytic activity for pure BZO and Bi doped BZO. In both cases the photocatalyst efficiency depends strongly of Bi content as well induced defects[13]. Recently, we have reported first order Raman modes for BZO system synthesized by microwave-assisted hydrothermal (MAH)[7] method assigned to local disorder, which are responsible by its emergent optical features. In addition, others optical properties have been discovered such as the conversion of ionizing radiation into visible light for BZO obtained by the same methodology[14].

The exploration of optical transitions covers a broad range of luminescent applications of perovskite based materials, increasing the interest and design of these functional materials. Introducing a small amount of foreign elements (usually transition metals or rare-earth element)[15] into the conventional metal oxide or to make solid ternary solid solution,

---

[a] *CCAF, Instituto de Física e Matemática (IFM), Departamento de Física, Universidade Federal de Pelotas, Campus do Capão do Leão, Caixa Postal, 354, CEP 96010-970, Pelotas, RS, Brazil. Fax: +55 53 3275-7614; Tel: +55 53 3275-7614; E-mail: mlucio3001@gmail.com*

[b] *CCAF, Graduate Program in Science and Materials Engineering, Technology Development Center, Federal University of Pelotas, 96010-900 Pelotas, RS, Brazil.*

[c] *Departament de Química Física i Analítica. Universitat Jaume I, Campus de Riu Sec, Castelló E-12080, Spain.*

[d] *Instituto de Física de São Carlos, USP, PO Box 369, 13560-970 São Carlos, SP, Brazil.*

[e] *INCTMN, Department of Physical Chemistry, Institute of Chemistry, Unesp - Universidade Estadual Paulista, Prof. Francisco Degni Street, s/n^o, Quitandinha, Araraquara, SP, 14800-900, Brazil.*

which can display compositionally tunable properties, are well known strategies used to manipulate the band gap value[16]. The dopant's may generate new energy levels between the valence band (BV) and conduction band (CB) of the metal oxide resulting in a reduced minimum light absorption energy gap of the host lattice. This process is capable to tailor the electronic structures by establishing new energy bands or localized impurity levels into the band gaps, and thus to extend the light-response range. Then, it is the key for the appearance of new properties and the potential applications have pushed forward increasing demands of more systematic and profound understanding on, say, crystalline structures and transformations among the polymorphous, defect and coordination chemistry, symmetries of local environments surrounding dopant's and so on.

MAH method has demonstrated its efficiency in the synthesis of materials with new and/or intensified properties[17–21]. The advantages of this synthesis method are the strong reduction over the time and temperatures even compared with hydrothermal and/or solvothermal conventional methodologies[22,23]. Other relevant aspect is the microwave radiation action producing besides the temperature increase, also rise the ionic conduction, charge polarization and possible hot spots throughout the solution[24,25]. All these intrinsic features of microwave heating are able to be responsible for local and/or periodic distortions, together or separately. In this respect, we present the first study of the effects on Hf-doped BZO material, by using he MAH method, to obtain $BaZr_{1-x}Hf_xO_3$, $x = 0.01$, 0.02, 0.04, 0.08 and 0.16, (BZHO) solid solutions. To truly understand the both short and large-range structures, different experimental techniques as well as first principle calculations have been carried out. The results are correlated with two techniques probing the local features of structure and bonding, i.e., X-ray absorption near-edge spectroscopy (EXAFS) and Raman spectroscopy[26]. These techniques complement x-ray diffraction (XRD) measurements. The XANES is able to determine the chemical surrounding (e.g., crystal field, density of unoccupied states, and the orientation of the specimen with respect to the polarization of the photon)[27,28]. Typically, measurements are made in transmission mode if attenuation length of the photon in the material being analysed is sufficiently long; however, in the soft X-ray region, due to small attenuation length, XANES measurements are made by detecting total electron yield (TEY), which is surface sensitive[29]. In the case of BZHO the absorptions of Zr K-edge and Hf L_{III}-edge can be obtained by XANES/EXAFS transmission mode, while for Ba L_{III}-edge and Zr L_{III}/L_{II}-edge the TEY methodology is more appropriated to operating condition of National Synchrotron Light Laboratory (LNLS). The X-ray absorption spectroscopy (XAS) has been applied in many case to investigate the local distortions of BZO perovskite[26,30]. On the other hand, Raman spectroscopy is able to investigate the polarizations of both asymmetric and symmetric bonds into the crystal[31], and first-order vibrational modes can be used to study local distortions[26].

2 Methods and Model Systems

MAH method i.e. hydrothermal synthesis under microwave radiation was developed as follows: firstly the concentrations of Hf atom were chosen obeying the "2^n" model, where "n" is the ordinal number and the result correspond to the Hf atom concentration. Then, with $n = 0$ the Hf concentration is 1%, with $n = 1$ is 2%, and so on. All precursors were metal chlorides and have the analytical grade in order of 99%. Each precursor was diluted in double deionized water under constant stirring at 50°C to avoid and/or prevent the carbonate formations. The molar concentrations of host matrix is 0.01054 mol/L for Ba and Zr atoms, being the Hf concentration a molar percentage of Zr with $n = 0$, 1, 2, 3 and 4. After mixed, the precursors were co-precipitate by KOH at 6 mol/L and immediately transferred to closed 110 mL polytetrafluoroethylene vessel, placed into microwave system.

Microwave system applies 2.45 GHz of radiation (Support information S1) with a maximum output power of 800 W. The reaction mixture was heated to 140°C in less than 1 min (at 800W) by a direct interaction between water molecules and microwave radiation, keeping at this temperature for 160 (BZO160) min under pressure of 2.5 Bar. Afterwards the microwave annealing the final white powders were washed by double deionized water till pH = 7 and finalized by absolute ethanol straining. The powders were dried at 80°C over night (around 12 h) in stove.

Several experimental characterization techniques were carried out, as X-ray diffraction by Rigaku DMax 2500PC using Cu $K_{\alpha 1}$ (λ = 1.5406 Å) and Cu $K_{\alpha 2}$ (λ = 1.54434 Å) radiation. The Raman spectra were recorded on a RFS/100/S Bruker Fourier transform Raman (FT-Raman) spectrometer with a Nd:YAG laser providing an excitation light at 1064 nm in a spectral resolution of 4 cm^{-1} and keeping its maximum output power at 85 mW. To analysis the morphology and crystal growth orientations the scanning electron microscope Zeiss VP Supra 35 equipped with a field emission gun (FE-SEM) and transmission electron microscope high resolution (TEM) Philips CM200, 200 kV with microanalysis. For XANES was chosed the Zirconium K and L_{III}-edge X-ray absorption and the spectra were collected at the LNLS (National Synchrotron Light Laboratory) facility using the D04B-XAFSII and D04A-SXS beam lines respectively. The LNLS storage ring was operated at 1.36 GeV and 160 mA. The Zirconium K-edge XANES and EXAFS spectra were collected in transmission mode at room temperature while in the soft x-ray region, due to small attenuation length, the Zr L_{III}-edge XANES measurements are made by detecting total electron yield (TEY), which is surface sensitive. UV-visible absorption was recorded using the Cary 5G spectrometer in total reflection mode by the integration sphere in region of 200 till 800 nm. All measurements were taken at room temperature.

The periodic density functional theory (DFT) method, applying the B3LYP functional[32–34] to take into account both exchange and correlations integration, has already been successfully employed[35,36] by using the CRYSTAL06 package code[37]. To control the accuracy of the Coulomb and exchange integrals were set to 10^{-8} (ITOL1 to ITOL4) and 10^{-14} (ITOL5), whereas the percentage of Fock/Kohn-Sham matrix mixing was set to 40 (IPMIX = 40). The reciprocal space was generated according to a regular sub-lattice determined by the shrinking factor which was set to 6 (13–20 independent k-points in the irreducible part of the Brillouin zone)[37].This methodology is well recognized by its performance to simulate electronic and geometric properties of materials with significant accuracy. The atomic centers have been described by all electron basis sets for Ba and Zr atoms (available from http://www.tcm.phy.cam.ac.uk/ mdt26/crystal.html) and 6-31G* for O atom.

Initially, an optimization of the lattice parameter has been performed, from this optimized structure, a 2 x 2 x 2 supercell was constructed to represent a doped superstructure with specific content of Hf atom. To construct the supercell, a model of imperfect crystals to cubic primitive (*P*) cell[38] was employed. In our case one Zr atom was replaced into the supercell resulting in 12.5% of Hf atom into BZO host lattice. It should be emphasized that the amount of Hf are based on previous semi-quantitative microanalysis results of our samples (to be addressed later). Accuracy factor were the same described previously always aiming the total energy minimization. After the simulation the band structure and density of states were obtained using ANA package code.

3 Results and Discussion

3.1 X ray and Raman

As it was commented, a staggered bottom-up structure was made-up by BZO host matrix doped with Hf under concentrations of 1, 2, 4, 8 and 16%, obeying the kinetic model 2^n, being $n = 0$, 1, 2, 3 and 4. The powder diffraction patterns can be analysed from the Figure 1, to which is easily noted the absence of significant amount of secondary phases, even for higher Hf concentration. For samples doped with 4, 8 and 16%, a very weak peak at $2\theta = 24°$ associated with the most intense diffraction of the witherite phase (barium Carbonate) can be observed, however any Hf secondary phases were detected. This indicates that even a large concentration as 16%, Hf can be considered as soluble into BZO lattice since there is no phase segregation of Hafnium compounds. In addition,

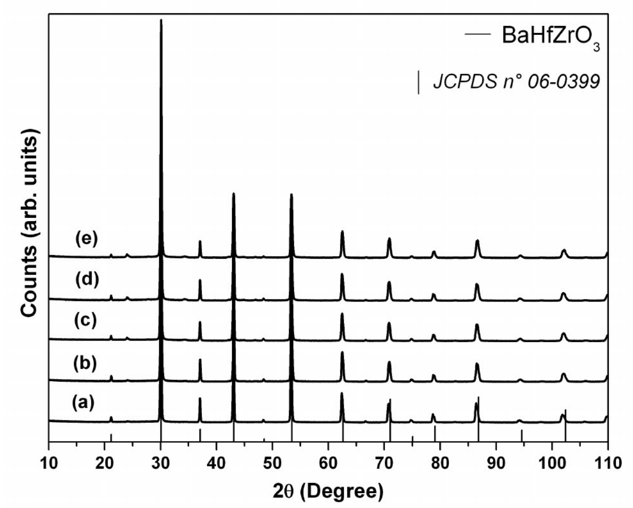

Fig. 1 X ray diffraction of pure BZO and BZO doped wth (a) 0%, (b) 1%, (c) 2%, (d) 4%, (e) 8% and (f) 16% of Hafnium

substantial changes in the BZO diffraction pattern assigned with $Pm\bar{3}m$ space group as a cubic structure, are not sensed. The main peak evidenced in the Figure 2 show a small displacement to high angles, moreover this behaviour indicates distortions in the host lattice.

An analysis of the X-ray diffractions patterns denotes that it is not capable to determinate if the Hf content was well introduced into the BZO lattice because the absence of perceptible changes in the diffraction pattern. Then, it is mandatory to use an analytical approach associated to different spectroscopy to determine the real concentration of Hf in each case.

For pure BZO or doped BZHO, any first order Raman spectrum is expected at room temperature because of all atoms in its structure occupying sites with inversion symmetry, and it, indeed, showed by X-ray patterns corresponding to the $Pm3m$ space group. The cubic paraelectric phase allows 12 optical modes ($3F_{1u} + 1F_{2u}$) that are not Raman active[39]. Meanwhile, the Raman spectrum of BZO and BHZO showed weak bands (at 277, 352, 462, 644, 707, 739, 846 and 1016 cm^{-1}). A slight local distortion of the oxygen octahedra can result in the breakdown of Raman selection rules, thereby giving rise to weak bands in the Raman spectrum associated to slight changes into the host lattice, in agreement with the previous reports.[31,40]. To this end, were measured samples with and without Hf contents for further analysis of differences among them. Raman active modes can be viewed in Figure 3, in which even small amounts of Hf yield substantial changes for all peaks compared with pure BZO spectrum. It is important emphasize that the crystal symmetry of BZO and BZHO samples continue to be cubic and do not should be measured any active Raman modes if the symmetry is kept perfect, or at least

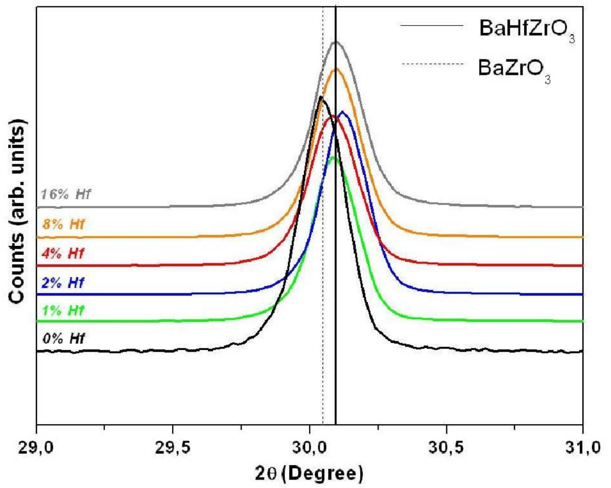

Fig. 2 Magnification of main diffraction peak (110), evidencing the displacement between pure BZO and BHZO doped with Hafnium.

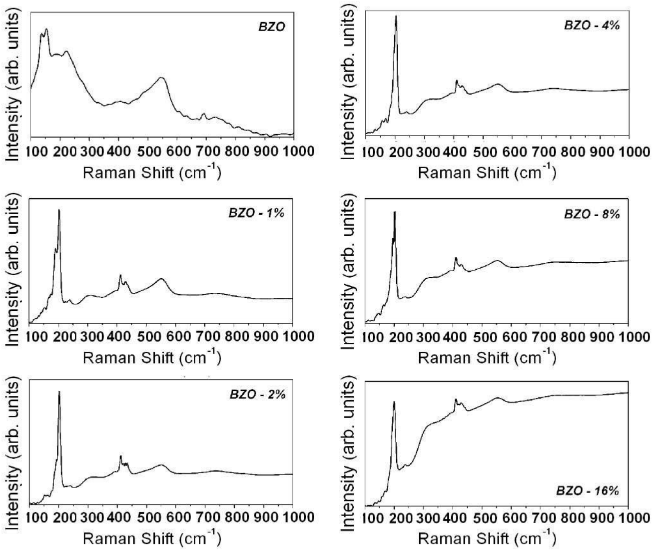

Fig. 3 Room temperature Raman spectroscopy for BZO samples with Hafnium under concentrations from 0 until 16%

Table 1 Theoretical (Theo) and experimental Raman modes for BZO and BHZO associated to its specific vibrations.

BZO	BHZO	BZO	BHZO	Vibration
Experimental		Theoretical		
—	—	101 (F2G) (B)	103 (F2G) (B)	Ba-O
129	—	116 (F2G) (B)	120 (F2G) (B)	Ba-O
152	162	159 (EG) (S)	161 (EG) (S)	Ba-O
191	198	195 (AG) (B)	189 (AG) (S)	Ba-O
225	241	—	—	
—	319	329 (F2G) (B)	329 (F2G) (B)	Ba-O
—	334	—	333 (F1G) (B)	Ba-O
337	—	338 (F2G) (B)	338 (F2G) (B)	O
396	393	—	—	
—	409	—	—	
457	433	—	—	
490	492	494 (F2G) (B)	492 (F2G) (B)	Ba-O
549	554	553 (F2G) (B)	551 (F2G) (B)	Zr-O, Hf-O
—	—	638 (EG) (S)	631 (EG) (S)	O
688	—	644 (BG) (S)	645 (EG) (S)	O
736	744	757 (AG) (S)	730 (AG) (S)	Ba-O
—	—	861 (EG) (S)	857 (EG) (S)	Ba-O
—	—	—	901 (AG) (S)	
—	—	920 (EG) (S)	920 (EG) (S)	Ba-O

almost perfect. Thus, all actives Raman modes must be associated to lattice imperfections, i.e. distortions of the ideal structure at short-range.

An analysis of the results depicted in Figure 3 renders that pure BZO has active modes and the values of each active vibrational mode are listed in the Table 1. The results point out that the main changes of calculated data correspond to the vibrations of the dopant site, just as a result of the replacement of Zr by Hf. Hafnium does not change the lattice symmetry as a whole but it does locally, i.e. change the short-range structure as it can be sensed in both theoretical and experimental values.

The activation of Raman transverse (TO) and longitudinal (LO) modes suggests that the concentration of these point defects is significantly higher than in samples prepared by other synthesis methods, in which active Raman modes were not observed. To better understand the origin of these vibrations, assigning the bands with they belongs and what kind of vibration, it is necessary to simulate these Raman modes. We have used DFT through of B3LYP functional. For pure BZO, an analysis of the results indicates that the experimental modes located around 129, 191 cm^{-1} can be related to molecular vibrations of transverse TO modes, while the modes located at 457 and 549 cm^{-1} are attributed to longitudinal and transverse vibrations, respectively, which can be considered as the first order. Besides of these modes, more one second-order experimental vibrational modes located at 225 cm^{-1} were observed[41]. Supplementing the set of vibration identified for pure BZO spectrum of still observed modes related to barium carbonate in 153 and 695 cm^{-1}. For BZHO the experimental vibration 195 cm^{-1} was observed a little displacement in relation to 191 cm^{-1} for pure BZO. On the other hand the vibrations at 129 cm^{-1} is absent for doped samples. This modes still belongs to TO vibrations but the displacement and absence are a result of introduction of Hf in the host lattice. The same behaviour can be observed to vibrations located at 433 cm^{-1} and 554 cm^{-1} for BZHO. Besides the second-order vibration was also displaced and for BZHO is located at 241 cm^{-1}. The Raman spectra for the BZHO can be simulated individually analysed and compared with that obtained for the pure BZO using the Table 1.

The simulated vibrational modes are in good agreement with the experimental results, although there are some modes not foreseen theoretically and some predicted modes that could not be observed. This fact is due to simulation takes into account only the primitive form of the structure as it was introduced, neglecting possible structural distortions not included in this model.

There are almost four vibrational modes that should be highlighted, being two stretching modes located around 159 and 192 cm^{-1} and two bending modes at 494 and 551 cm^{-1}. These modes appear in both structure and are not significantly modified by the introduction of Hf. Moreover modes located around 300 cm^{-1} are strongly affected causing even that two nearby frequencies are present, one only in the pure sample and another one in BZHO sample. Changes on crystal field incorporated by Hf content leads to a bending mode at 334 cm^{-1} on Ba-O vibration. However the effective participation of Hf is only detected by the simulations for the mode located at 333 cm^{-1}.

3.2 Theoretical model, band structure and density of states

The calculated total and the partial density of states (DOS) are depicted in Figures 4 and 5, which reports the slight contribution of 5*d* orbitals of Hf to the CB region. To perform the Hf content into the BZO host lattice, the supercells $(2 \times 2 \times 2)$ were built as show in Figure 6A. The simulated Hf content was 12.5%, matching to the high experimental concentration. In this case the DOS intensity of Hf was intensified ten times to the better representation its 5*d* states contribution. A detailed analysis for the Figures 4 and 5 renders that the modification over the relative intensity of total DOS at CB above 6 eV, can be associated to the superposition of 4*d* (Zr) and 5*d* (Hf) states. Significant changes can be sensed in the oxygen 2*p* region, related to the interactions of electronic density of states of hafnium 5*d* and oxygen 2*p*, which only can be noted by means of the convolution with the XAS techniques. Still into CB for all projections the low intensity of the projections just above the band gap leads to an idea that the gap is even greater, however projections in this region are not observed only due to its low contribution, but it does not nonexistent.

The calculated energy band structure of cubic BZO and BZHO samples along the high-symmetry points of the Brillouin (see Figure 6B) supply arguments to discuss the host BZO lattice polarizations as Hf was added. For both situations the top of the VB is taken as the zero of energy jointly with Fermi level. BZHO band structure corresponds to the 12.5% of Hf content into the BZO system, as it in depicted in the Figure 6B. A careful inspection over BZHO band structure shows clearly the introduction of states at CB located above of 6 eV, although in the VB the distributions changes are almost undetected.

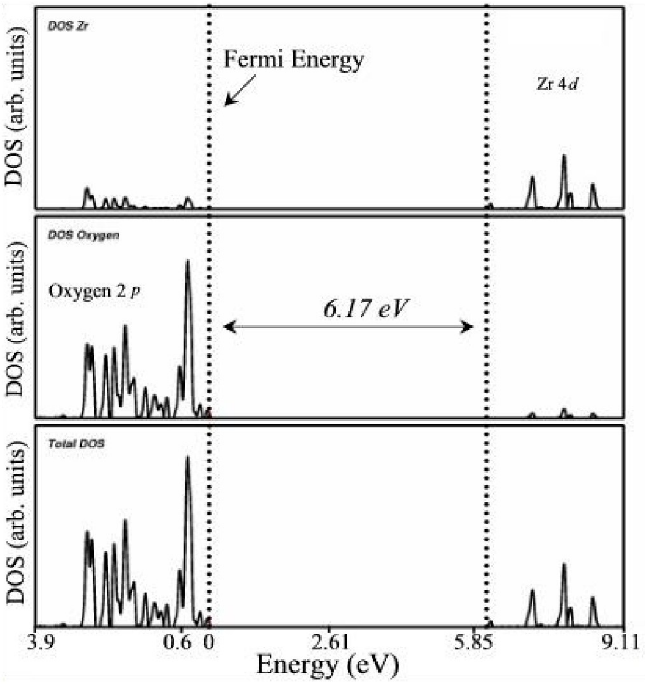

Fig. 4 Projected density of states of zirconium, oxygen and total DOS for pure BZO sample

The slight scroll down energy on the CB states can be explained as the superposition between 4*d* and 5*d* states of Zr and Hf atoms, respectively. In this case the 5*d* states are located at lower energies than those corresponding to Zr, leading to slightly decrease in the calculated band gap from 6.17 to 6.12 eV. This band gap originates from a transition from O 2*p* filled electron states located at the top of the VB to the mixed empty Zr 4*d* and Hf 5*d* electron states dominating the bottom of the CB. Previous calculations showed the direct band gap of $BaHfO_3$ is around 3 eV[42].

3.3 X ray absorption near-edge spectroscopy

To support the results obtained from theoretical simulations, XANES was deeply used as will be report hereafter. Firstly, is necessary the confirmation if Hf is replacing Zr and/or Ba into the BZO lattice. Zirconium K and L_{III}-edge spectra shown in Figures 7, 8 and 10 were analysed jointly to barium L_{III}-edge present in Figure 9. In the zirconium K-edge is not easily observed significant changes, unless by a subtle green line signal apparent at such parts of the spectra, corresponding to BZO undoped sample. Zr K-edge XANES spectra of crystalline BZO and BZHO compounds are depicted in Figure 7. For BZO and BHZO systems, Zr is 6-coordinated to oxygen atoms into octahedral cluster and the main edge is split into two well

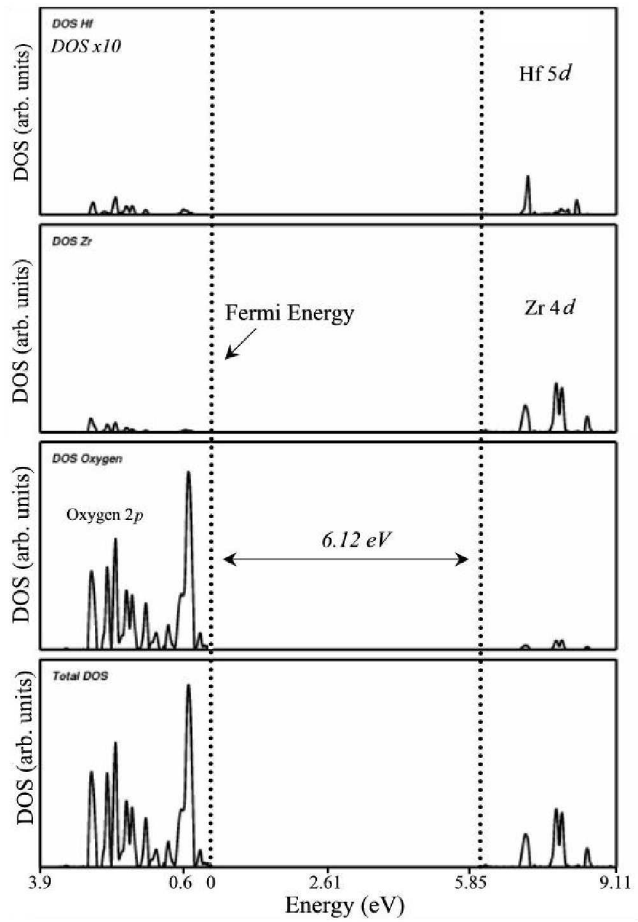

Fig. 5 Projected density of states of hafnium (x10), zirconium, oxygen and total DOS for BHZO sample.

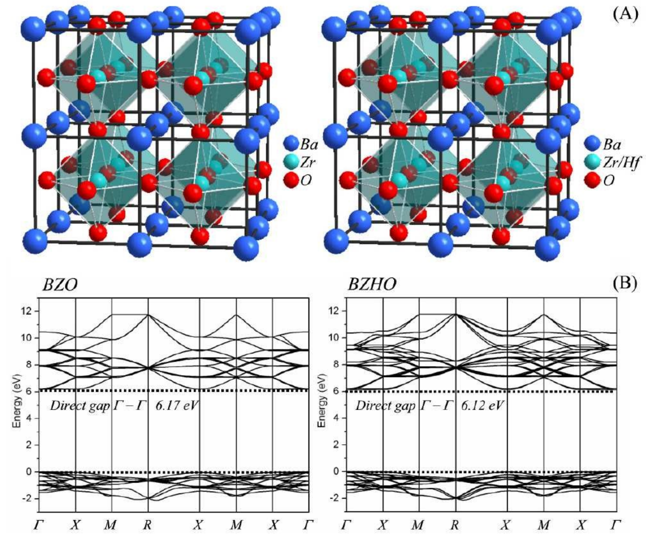

Fig. 6 In (A) schematic 3D cubic structure evidencing the octahedral sites for zirconium and hafnium for pure and doped samples. In (B) are report the band structure denoting the top of valence band and button of conduction band for pure and hafnium-doped BZO.

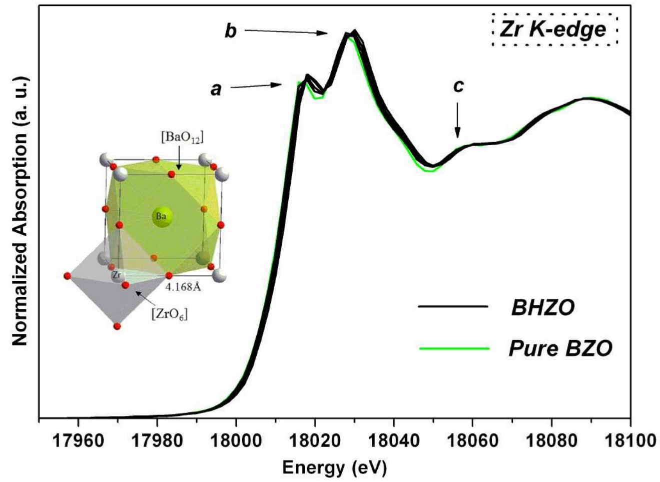

Fig. 7 Zirconium K-edge for BHZO and pure BZO evidencing the peaks “a”, “b” and “c” where are the mainly differences among the pure and doped samples.

resolved features, “a” at 18018.5 eV and “b” at 18030.0 eV[27]. The more intense peak of the Zr K-edge match with “b” feature. This assertion was confirmed by the XANES simulations performed by Giannici et. al[43], taking into account two environments for Zr. Additionally at 40 eV after "white line" (first absorption) is evident a wide shoulder, which is absent to ZrO_2 due to its tetrahedral environment. The existence of this supplementary shoulder is reported as a strong correlation Zr-Zr and/or Zr-Ba and subsequently multiply scattering for octahedral environment as naturally expected to BZO and BZHO samples[28].

The main distinguished "white lines" are evident for zirconium L_{III}-edge, denoted by the intensity relationships between peaks “*A*” and “*B*” identified in the Figure 8. The height of Zr L_{III}-edge features has been shown to be related to the geometry of Zr-oxygen polyhedra[44,45] and hence with its local distortions. Therefore, any change in the cluster environment alters the electronic structure of the absorbing atom and should be reflect in the corresponding optical properties results. Acquired spectra were measured at 25°C, in which the cubic structure for BZO is the thermodynamically stable phase, even for high doped samples as 16% of Hf. The cubic structure was kept, although the Hf 5*d* orbitals introduce a tendency to weak field support the increased of typical $d-splitting$ for Zr L_{III}-edge from 2.3 to 3.1 eV between A and B peaks for cubic BHZO local environment[27]. Is important to note that the 2.3

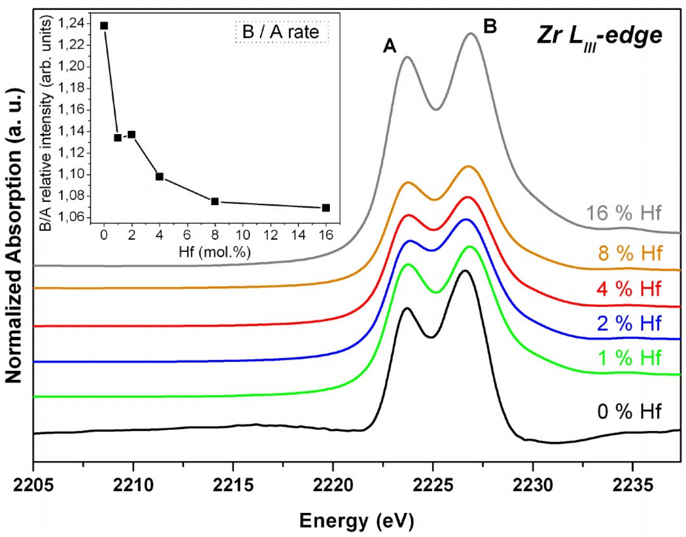

Fig. 8 Zirconium L_{III}-edge for peaks A and B reporting the E_g and T_2G contribution for L_{III}-edge. The inset denotes the B/A ratio.

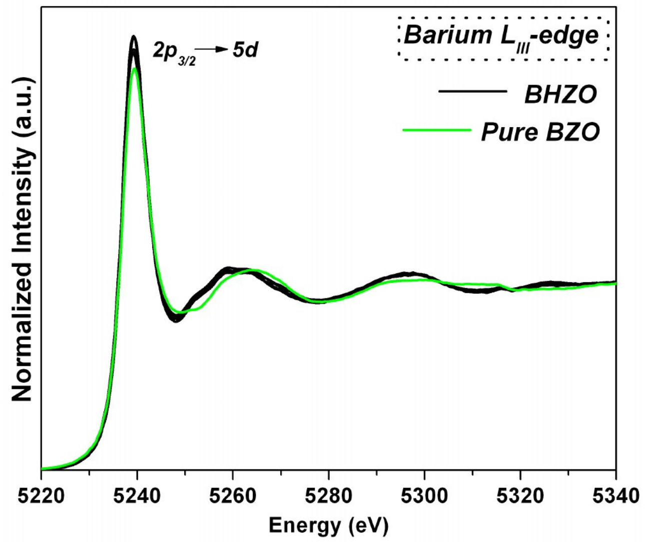

Fig. 9 Barium L_{III}-edge for pure and BHZO samples.

eV split are related to tetrahedral crystal field. In our samples we have a octahedral crystal field, then the splitting increase a expected by the crystal field theory to 3.1 eV. A careful analysis of Figure 8 shows that the Zr L_{III}-edge of BZO is characterized by two main distinctive features, which correspond to split between the signals of orbitals levels xy, yz and xz for t_{2g} and z^2, $x^2 - y^2$ for e_g situated into the Zr edge represented by peaks A and B, respectively[46]. The separation of t_{2g} and e_g orbitals is related to crystal-field splitting effect denoted by electronic transitions from the occupied O $2p$ orbitals to the empty Zr $4d$ and/or Hf $5d$ orbitals as it was demonstrated in the theoretical modelling section. From the viewpoint of Zr local symmetry, all samples has a octahedral crystal field symmetry (Oh point group) report random disordered ZrO_6 octahedron into cubic structure because the relative intensity between A and B peaks is different for each sample, most probably as a result of Hf presence.

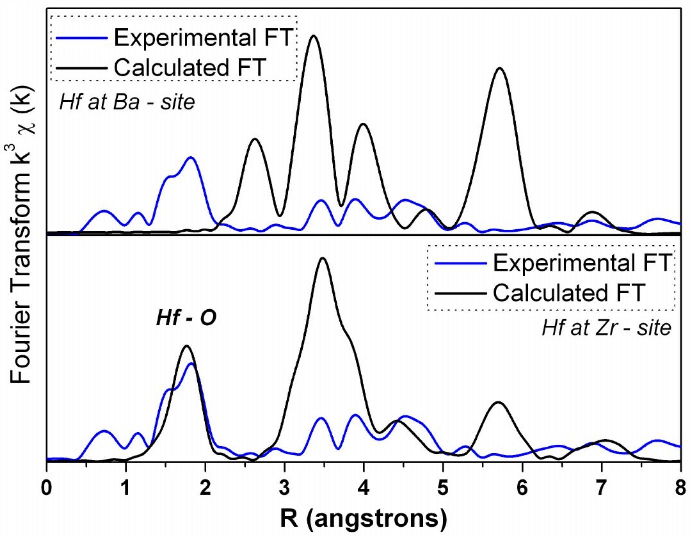

Fig. 10 Experimental and theoretical Fourier transformer of first coordination sphere to identifies the location of Hafnium in to the BZO host lattice. The simulation were performed to Hf in substitution of Ba and Zr.

For cubic systems the relativity intensity between A and B peaks obeys the B/A rate higher than unity. The B/A relationship for pure BZO and BZHO samples are displayed into the inset of Figure 8. For Ba L_{III}-edge in Figure 10 no difference can be sensed among BZHO doped samples, even under 16% of Hf content into BZO host lattice. On the other hand, for undoped samples there are significant variations on XANES region. Then, it is mandatory to employ a more careful analysis on the Hf L_{III}-edge to determine the Hf replacements.

To this end, a comparison between experimental data and simulated EXAFS for 16% of Hf replacement over Ba and Zr sites has been performed. EXAFS spectra were calculated by supposing the substitution of either Ba or Zr by Hf atoms in the Hf L_{III}-edge. The Figure 10 evidence the Fourier Transform (FT) for each situation, the first FT peak corresponds to the first Hf-O coordination shell while the other peaks are related to further Hf-coordination shells.

As observed in Figure 10, the simulated EXAFS spectrum for Hf oscillations located at Zr octahedral sites is quite similar to the experimental data, whereas the EXAFS spectrum of Hf at Ba cubooctahedral sites is completely different. Then, Hf element is preferentially located in octahedral sites replacing

Zr atom.

3.4 Microscopy and Microanalysis

The scanning images provide information to evaluate the microscopic possible influence of dopant contents over shape and size of the samples. A detailed analysis of the results shows that the shape of decaoctahedral BZO was slight affected by increase of Hf amount. In Figure 11 the smoothing effect of the decaoctahedral edge between adjacent facets is evident, i.e. a morphological change takes place, from decaoctahedral shape to form a quasi-spherical assembled particle as increases the Hf content. We can also observe that the self-assembled process become more evident, probably due to the slight increase of individual nanoparticles. Recently, we have observed a reversed crystal growth process to pure BZO compound as a result of competition between self-assemble and Oswald ripening processes[47]. In this case the introduction of Hf seems to prevent the Oswald repining, due to increased growth of individual grains or/and by homogenization of the grain size distribution, avoiding a great reversed crystallization process as observed to pure BZO[47].

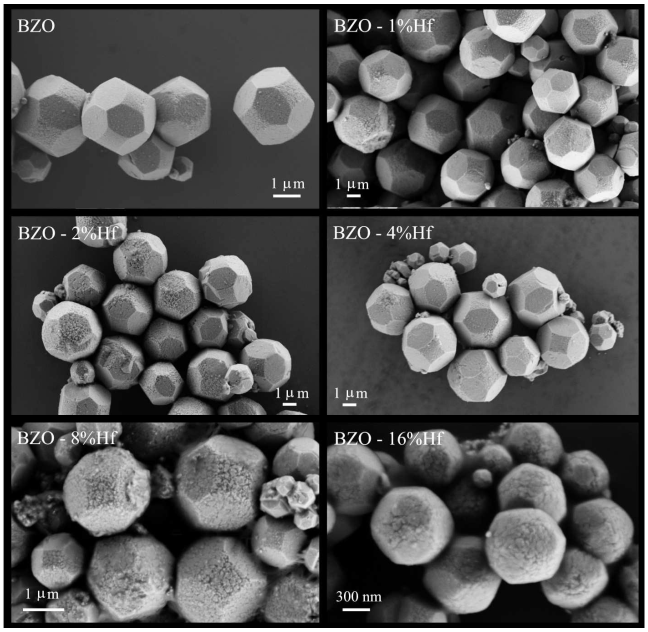

Fig. 11 FE-SEM images of decaoctahedral BZO and the surface smoothing for samples doped with hafnium.

One way to estimate the Hf content is microanalysis performed by FE-SEM. In the Table 2 the Hf concentration proposed and results obtained from microanalysis are presented. An analysis of these results allow us conclude that the Hf was well included into the BZO host lattice for all concentrations until 8%, except to 16%, which report only 12,5 ∼ 13% of Hf. Then, this result allows us to use the largest concentration of Hf to carry out the simulations.

Table 2 FE-SEM Microanalysis for BZO and BHZO samples.

Samples	Nominal Hafnium content (%)	Microanalysis (%)
BZO	0	0
BHZO - 1%	1	2.45
BHZO - 2%	2	2.72
BHZO - 4%	4	3.88
BHZO - 8%	8	7.28
BHZO - 16%	16	12.34

TEM reveals a mesocrystalline feature of the BHZO sample with 13% of Hf as indicated by microanalysis. It's important note that the interplanar distance d = 0.303 nm was not changed if compared to pure BZO lattice as can be seen in Figure 12b. The decaoctahedral shape are still easily identified for same particles in the bright field image 12c for sample BZHO with 16% of Hf, however in the Figure 12d the most part of the particles have a tendency to the spherical shape.

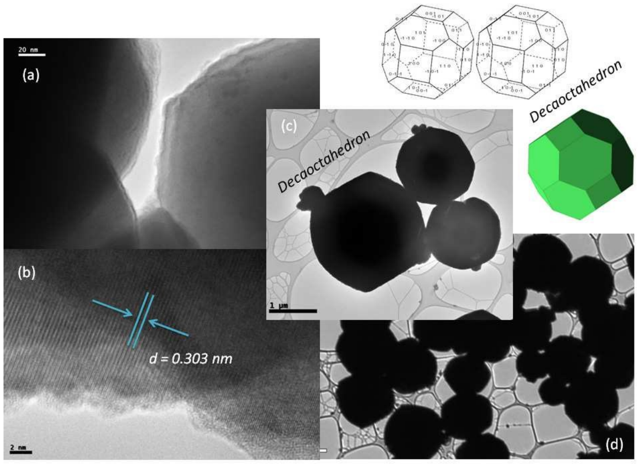

Fig. 12 Transmission electron microscopy of decaoctahedral BZO evidencing the typical d-spacing of BZO associated to the schematic model to surface (hkl) exposed.

4 Conclusions

In summary, the main conclusion of the present work can be summarized as follows: i) By means of MAH method, we have successfully introduced Hf into the $BaZrO_3$ (BZO) host lattice to form a solid solution $BaZr_{1-x}Hf_xO_3$, $x = 0.01$, 0.02, 0.04, 0.08 and 0.16, BZHO. Hf^{4+} ions are successful introduced in perovskite-type cubic structure to substitute for Zr^{4+} ions on the 6-fold coordination. ii) The periodic structure, i.e. long-range structure was not strong affected by the Hf introduction, while the local symmetry, i.e. short-range structure was modified and hence the electronic structure presents a new behaviour. iii) TEM analysis point out the mesocrystalline nature of self-assembled BZHO nanoparticles under decaoctahedral shape. iv) XAS patterns are able to determine in which site Hf was introduced in the host lattice and assign short-range distortion on Zr-O and Hf-O bonds. v) Band structures corroborate XAS results showing the split on states of conduction band due to 5d orbitals of hafnium. By density of states is observed a low contribution of 5d orbitals. However they are capable to introduce the split on band structure. vi) The introduction of the 5d states changes the polarization of structure modifying the original Raman mode. These is confirmed by the good correlation found between simulated and experimental Raman results. vii) This features can be use to interpret the electronic and optical properties of this system as a luminescence emission at room temperature for crystalline perovskites.

Acknowledgments

The authors are grateful to Mr. Rorivaldo Camargo for operating the FE-SEM equipment. We also are very grateful to LNLS, Campinas, SP, Brazil was this research was partially performed. We acknowledge the financial support of the Brazilian research funding institution FAPESP (2009/17752-0), FAPERGS (2031-2551/13-9SIAS) and CNPq (MCT/CNPq 458452/2014-9). J. Andrés acknowledges Generalitat Valenciana (Prometeo/2009/053 project), Ministerio de Ciencia e Innovación (project CTQ-2012-36253-C03-01) Programa de Cooperación Científica con Iberoamerica (Brazil), Ministerio de Educación (PHB2009-0065-PC).

References

1 J. Suntivich, H. A. Gasteiger, N. Yabuuchi, H. Nakanishi, J. B. Goodenough and Y. Shao-Horn, *Nature chemistry*, 2011, **3**, 546–550.

2 Y. Zhao, L. Xu, L. Mai, C. Han, Q. An, X. Xu, X. Liu and Q. Zhang, *Proceedings of the National Academy of Sciences*, 2012, **109**, 19569–19574.

3 N. A. Benedek and C. J. Fennie, *The Journal of Physical Chemistry C*, 2013, **117**, 13339–13349.

4 S. V. Bhide and A. V. Virkar, *Journal of the Electrochemical Society*, 1999, **146**, 4386–4392.

5 I. Antunes, G. Mather, J. Frade, J. Gracio and D. Fagg, *Journal of Solid State Chemistry*, 2010, **183**, 2826–2834.

6 L. Cavalcante, V. Longo, M. Zampieri, J. Espinosa, P. Pizani, J. Sambrano, J. Varela, E. Longo, M. Simoes and C. Paskocimas, *Journal of Applied Physics*, 2008, **103**, 063527.

7 M. L. Moreira, J. Andrés, J. A. Varela and E. Longo, *Crystal Growth and Design*, 2009, **9**, 833–839.

8 R. Borja-Urby, L. Diaz-Torres, P. Salas, M. Vega-Gonzalez and C. Angeles-Chavez, *Materials Science and Engineering: B*, 2010, **174**, 169–173.

9 Z. Lu, Y. Tang, L. Chen and Y. Li, *Journal of Crystal Growth*, 2004, **266**, 539–544.

10 G. Łupina, J. Dabrowski, P. Dudek, G. Kozłowski, P. Zaumseil, G. Lippert, O. Fursenko, J. Bauer, C. Baristiran, I. Costina *et al.*, *Applied Physics Letters*, 2009, **94**, 152903–152903.

11 H. Huhtinen, K. Schlesier and P. Paturi, *Superconductor Science and Technology*, 2009, **22**, 075019.

12 S. H. Wee, E. D. Specht, C. Cantoni, Y. L. Zuev, V. Maroni, W. Wong-Ng, G. Liu, T. J. Haugan and A. Goyal, *Physical Review B*, 2011, **83**, 224520.

13 R. Borja-Urby, L. Díaz-Torres, P. Salas, E. Moctezuma, M. Vega and C. Ángeles-Chávez, *Materials Science and Engineering: B*, 2011, **176**, 1382–1387.

14 M. L. Moreira, D. P. Volanti, J. Andrés, P. J. Montes, M. E. Valerio, J. A. Varela and E. Longo, *Scripta Materialia*, 2011, **64**, 118–121.

15 T. M. Mazzo, M. L. Moreira, I. M. Pinatti, F. C. Picon, E. R. Leite, I. L. Rosa, J. A. Varela, L. A. Perazolli and E. Longo, *Optical Materials*, 2010, **32**, 990–997.

16 Y. Inaguma, T. Muronoi, K. Sano, T. Tsuchiya, Y. Mori, T. Katsumata and D. Mori, *Inorganic chemistry*, 2011, **50**, 5389–5395.

17 I. Bilecka and M. Niederberger, *Nanoscale*, 2010, **2**, 1358–1374.

18 A. Ristić, K. Lázár, H. Solt and V. Kaučič, *CrystEngComm*, 2011, **13**, 1946–1952.

19 N. Shojaee, T. Ebadzadeh and A. Aghaei, *Materials Characterization*, 2010, **61**, 1418–1423.

20 X. Wang, K. Qu, B. Xu, J. Ren and X. Qu, *Journal of Materials Chemistry*, 2011, **21**, 2445–2450.

21 H. J. Kitchen, S. R. Vallance, J. L. Kennedy, N. Tapia-Ruiz, L. Carassiti, A. Harrison, A. G. Whittaker, T. D. Drysdale, S. W. Kingman and D. H. Gregory, *Chemical reviews*, 2013.

22 G. J. Wilson, A. S. Matijasevich, D. R. Mitchell, J. C. Schulz and G. D. Will, *Langmuir*, 2006, **22**, 2016–2027.

23 H. Katsuki, S. Furuta and S. Komarneni, *Journal of Porous Materials*, 2001, **8**, 5–12.

24 M. A. Herrero, J. M. Kremsner and C. O. Kappe, *The Journal of organic chemistry*, 2008, **73**, 36–47.

25 W. C. Conner and G. A. Tompsett, *The Journal of Physical Chemistry B*, 2008, **112**, 2110–2118.

26 F. Giannici, M. Shirpour, A. Longo, A. Martorana, R. Merkle and J. Maier, *Chemistry of Materials*, 2011, **23**,

2994–3002.

27 L. Galoisy, E. Pélegrin, M.-A. Arrio, P. Ildefonse, G. Calas, D. Ghaleb, C. Fillet and F. Pacaud, *Journal of the American Ceramic Society*, 1999, **82**, 2219–2224.

28 G. Mountjoy, D. M. Pickup, R. Anderson, G. W. Wallidge, M. A. Holland, R. J. Newport and M. E. Smith, *Physical Chemistry Chemical Physics*, 2000, **2**, 2455–2460.

29 J. P. Ko, Y.-M. Yiu, H. Liang and T.-K. Sham, *The Journal of chemical physics*, 2010, **132**, 234701.

30 D. Andrault and J. Poirier, *Physics and Chemistry of Minerals*, 1991, **18**, 91–105.

31 P. Dobal, A. Dixit, R. Katiyar, Z. Yu, R. Guo and A. Bhalla, *Journal of Applied Physics*, 2001, **89**, 8085–8091.

32 A. D. Becke, *Physical Review A*, 1988, **38**, 3098.

33 E. Longo, E. Orhan, F. Pontes, C. Pinheiro, E. Leite, J. Varela, P. Pizani, T. Boschi, F. Lanciotti Jr, A. Beltran *et al.*, *Physical Review B*, 2004, **69**, 125115.

34 A. D. Becke, *The Journal of Chemical Physics*, 1993, **98**, 5648–5652.

35 V. M. Longo, L. S. Cavalcante, M. G. Costa, M. L. Moreira, A. T. de Figueiredo, J. Andrés, J. A. Varela and E. Longo, *Theoretical Chemistry Accounts*, 2009, **124**, 385–394.

36 M. L. Moreira, P. G. C. Buzolin, V. M. Longo, N. H. Nicoleti, J. R. Sambrano, M. S. Li, J. A. Varela and E. Longo, *The Journal of Physical Chemistry A*, 2011, **115**, 4482–4490.

37 V. R. S. Dosevi, *CRYSTAL06 user's manual*, University of Torino, Torino, 2006.

38 R. Evarestov and V. Smirnov, *Journal of Physics: Condensed Matter*, 1997, **9**, 3023.

39 R. Loudon, *Advances in Physics*, 1964, **13**, 423–482.

40 K. Dhahri, M. Bejar, E. Dhahri, M. Soares, M. Graça, M. Sousa and M. Valente, *Chemical Physics Letters*, 2014, **610–611**, 341 – 344.

41 H. Yamashita, S. Yamaguchi, M. Yokozeki, M. Nakashima and T. Maekawa, *Nippon seramikkusu kyokai gakujutsu ronbunshi*, 1999, **107**, 895–900.

42 A. Bouhemadou, F. Djabi and R. Khenata, *Physics Letters A*, 2008, **372**, 4527–4531.

43 F. Giannici, A. Longo, A. Balerna, K.-D. Kreuer and A. Martorana, *Chemistry of materials*, 2009, **21**, 2641–2649.

44 N. Thromat, C. Noguera, M. Gautier, F. Jollet and J. Duraud, *Physical Review B*, 1991, **44**, 7904.

45 J. A. Rodriguez, J. C. Hanson, J.-Y. Kim, G. Liu, A. Iglesias-Juez and M. Fernández-García, *The Journal of Physical Chemistry B*, 2003, **107**, 3535–3543.

46 F. Zhang, P. J. Chupas, S. L. A. Lui, J. C. Hanson, W. A. Caliebe, P. L. Lee and S.-W. Chan, *Chemistry of materials*, 2007, **19**, 3118–3126.

47 M. L. Moreira, J. Andrés, V. R. Mastelaro, J. A. Varela and E. Longo, *CrystEngComm*, 2011, **13**, 5818–5824.